Perspective

Polarized Raman Spectroscopy for Determining Crystallographic Orientation of Low-Dimensional Materials

Bo Xu, Nannan Mao, Yan Zhao, Lianming Tong,* and Jin Zhang*

Read Online

ACCESS | Metrics & More | Article Recommendations

ABSTRACT: Raman spectroscopy is a fast and nondestructive characterization technique, which has been widely used for the characterization of the composition and structure information of various materials. The symmetry-dependent Raman tensor allows the detection of crystallographic orientation of materials by using polarization information. In this Perspective, we discuss polarized Raman spectroscopy as a powerful tool for determination of the crystallographic orientation of various materials. First, we introduce the basic principles of polarized Raman spectroscopy and the corresponding experimental setups; the determination of crystallographic orientation of two-dimensional (2D) materials with in-plane isotropy and in-plane anisotropy using linearly polarized Raman scattering are then discussed. Furthermore, we discuss that using circularly polarized Raman spectroscopy, the azimuthal angle of materials in three dimensions (3D) can be characterized. In the final section, we show that the orientation distribution of nanomaterial assemblies can be measured using polarized Raman spectroscopy by introducing the orientation distribution function.
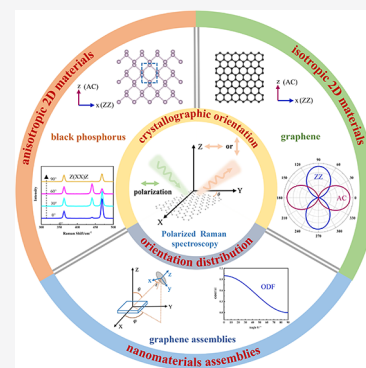
Raman spectroscopy has gained widespread popularity ranging from the characterization of materials to quality tests in recent years.[1−4] The detection limitation can be down to the single-molecule level through the technique of surface-enhanced Raman spectroscopy (SERS), which can significantly amplify the Raman scattering intensity.[5] Moreover, Raman spectroscopy is a powerful tool for characterization of doping, layer numbers, defects, disorder, and strain for 2D materials such as graphene, transition-metal dichalcogenides (TMDCs), and anisotropic black phosphorus (BP).[3] Specifically, the orientation can be detected through the polarization-dependent Raman intensities.[6−9]

The assembly of nanomaterials into macrostructures endows designed function to materials stemming from the superior physical and chemical properties of unit nanomaterials.[10−12] The performance of the macroscopic materials is closely related to their microstructures, where the orientation of unit nanomaterials is one of the most important factors.[13] Typical examples include carbon nanomaterial fibers, polymer nanocomposites, and photonic crystals.[14−17] Thus, the characterization techniques for the determination of orientation have been of great importance to understand the relationship between structure and performance in material science.

To date, various techniques have been used to characterize microscopic structures, including X-ray diffraction (XRD), transmission electron microscopy (TEM), scanning electron microscopy (SEM), and atomic force microscopy (AFM).[18−21] Among these techniques, Raman spectroscopy is a fast, effective, and nondestructive tool that has been widely applied. In this Perspective, we focus on the orientation character-

ization of low-dimensional materials including 2D materials and nanomaterial assemblies using polarized Raman spectroscopy.

> Raman spectroscopy is a fast, effective, and nondestructive tool that has been widely applied.

The Raman scattering efficiency is related to the Raman tensor **R** and the polarization configuration:[9]

$$ S = A\left[\sum_{k,l=x,y,z} e_i^k R_{kl} e_s^l\right]^2 = A|\vec{e}_s \cdot \tilde{R} \cdot \vec{e}_i|^2 \tag{1}$$

where Jones vectors $\vec{e}_i$ and $\vec{e}_s$ represent the polarization directions of incident and scattered light, respectively. For example, the Jones vector is $\binom{1}{0}$ or $\binom{0}{1}$ when the polarization of light is along the X or Y axis. For doubly degenerated Raman mode such as the G mode of graphene, the Raman scattering
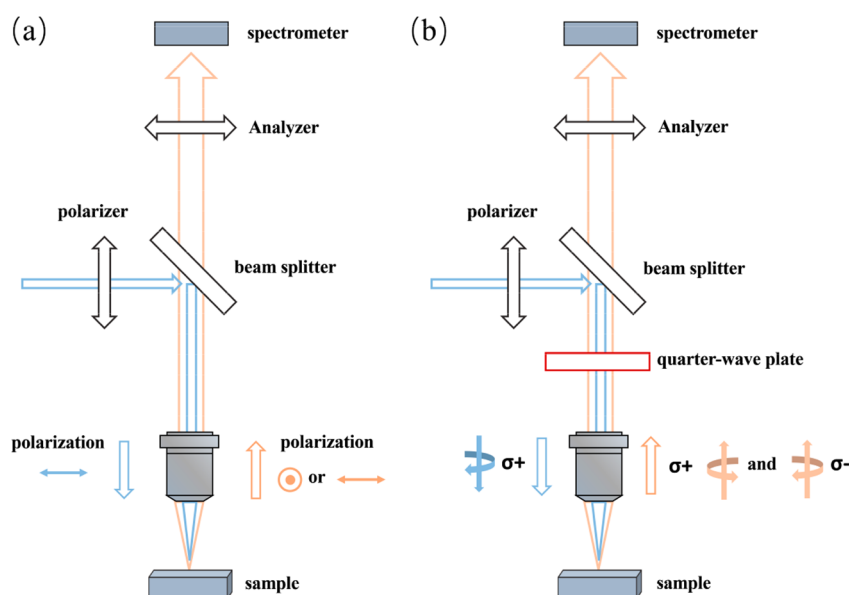
Figure 1. Schematic diagrams of typical polarization configurations for angle-resolved polarized Raman spectroscopy (a) and helicity-resolved Raman spectroscopy (b).

efficiency is the sum of the contribution of the two Raman tensors.

It should be noted that the coordinate system of Raman tensors must be consistent with that of the Jones vectors, because $\tilde{R}$ and $\vec{e}$ differ with respect to the coordinate systems. We define the laboratory coordinate system as O-XYZ and the specimen coordinate system as O-xyz. For linearly polarization light along the Z-axis, the Jones vector can be expressed as

$$\vec{e} = \begin{pmatrix} \cos\Phi \\ \sin\Phi \\ 0 \end{pmatrix} \qquad (2)$$

where Φ is the angle between the polarization and the X-axis. On the other hand, the orientation of the crystal can be expressed by the Euler angle $(\theta, \varphi, \varepsilon)$, where θ, φ, and ε are nutation angle, precession angle, and rotation angle, respectively. Therefore, the Raman tensor of the laboratory coordinate system (O-XYZ) can be written as

$$\tilde{R}(\theta, \varphi, \varepsilon) = r^t \tilde{R}_0 r \qquad (3)$$

where $\tilde{R}_0$ is the Raman tensor of the specimen coordinate system (O-xyz), r and r^t are the transformation matrix of coordinate systems and its transposed matrix[22]

$$r = \begin{pmatrix} \cos\theta\cos\varphi\cos\varepsilon - \sin\varphi\sin\varepsilon & -\cos\theta\sin\varphi\cos\varepsilon - \cos\varphi\sin\varepsilon & \sin\theta\cos\varepsilon \\ \cos\theta\cos\varphi\sin\varepsilon + \sin\varphi\cos\varepsilon & -\cos\theta\sin\varphi\sin\varepsilon + \cos\varphi\cos\varepsilon & \sin\theta\sin\varepsilon \\ -\sin\theta\cos\varphi & \sin\theta\sin\varphi & \cos\theta \end{pmatrix} \qquad (4)$$

Generally, the efficiency of Raman scattering can be expressed by

$$I(\theta, \varphi, \varepsilon, \Phi) \propto |\vec{e}_s(\Phi) \cdot \tilde{R}(\theta, \varphi, \varepsilon) \cdot \vec{e}_i(\Phi)|^2 \qquad (5)$$

So we can obtain the orientation of samples from the intensity of Raman scattering according to eq 5, which is the principle for the orientation determination. Specifically, the calculation will be much easier for low-dimensional materials such as graphene or carbon nanotubes where ε and ψ are invariables.

Angle-resolved polarized Raman spectroscopy (ARPRS) is an important branch of Raman spectroscopy. The typical polarization configuration is that the polarizations of incident light and scattered light are both along the x or y axis under backscattering conditions. Usually we use V (vertical) or H (horizontal) to separately denote the polarization directions of incident and scattered light, and the typical configurations (VV and HH) are as shown in Figure 1a. The polarization of incident light and analyzer direction can rotate separately with respect to the sample, and the sample can rotate in the plane as well. The three typical configurations of ARPRS include (a) to rotate the polarization of incident light, (b) to rotate the sample in the plane, (c) to set a half-wave plate in the common optical path to simultaneously vary their polarization direction, which have been described in detail in ref 23. Moreover, when excited by circularly polarized light, the Raman scattered light may also be circularly polarized with the same or different helicity as the incident light. The spectrum for detecting the helicity of Raman scattered light is termed helicity-resolved Raman spectroscopy (HRRS). The experimental setup is shown in Figure 1b.[24] HRRS is advantageous in characterizing the out-of-plane orientation because the in-plane orientation of materials has no influence on the helicity of the Raman scattering.[25]

Two-dimensional (2D) materials have attracted wide attention because of their unique properties distinct from their 3D counterparts. To date, various 2D materials have been produced and investigated, such as graphene, black phosphorus (BP), and transition-metal dichalcogenides (TMDCs). ARPRS and HRRS have played significant roles in 2D materials research; for example, ARPRS can be used to study the orientation as well as the Raman tensors for various 2D materials,[8,26−30] and HRRS has been used to characterize the excitonic nature and electron−phonon coupling for TMDCs.[24,31] From the in-plane symmetry point of view, these 2D materials can be divided into isotropic materials (graphene, MoS_2, h-BN, etc.) and anisotropic materials (BP, ReS_2, $ReSn_2$, etc.). For in-plane isotropic 2D materials, the mechanical, thermal, optical, and electric properties are
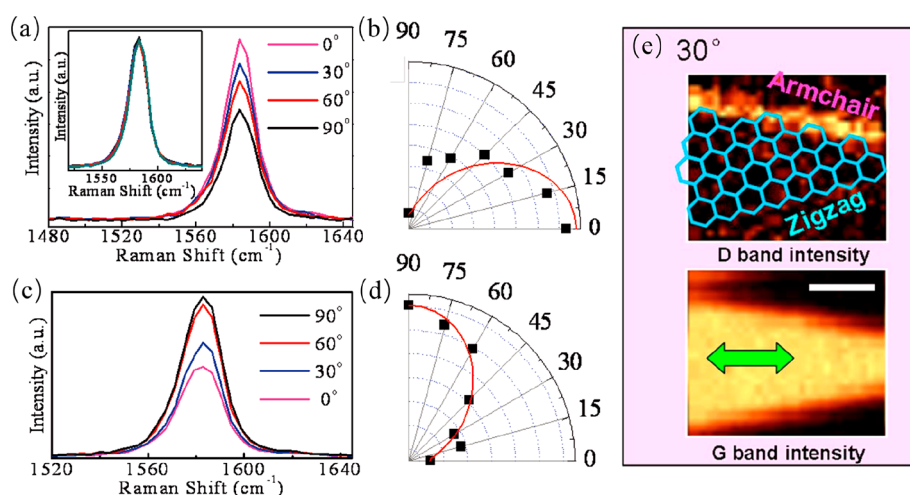
Figure 2. (a−d) Polarization dependence of G mode for armchair edges and zigzag edges. Typical Raman spectra for incident laser with polarization angles 0°, 30°, 60°, and 90° with respect to the armchair (a) or zigzag edges (c). Polar plots of the integrated intensity for the armchair (b) or zigzag edges (d).[36] (e) Raman images of D and G band intensities of graphene edges with 30° angle. The green arrow indicates the laser polarization and the scale bar is 1 μm.[37] Reprinted with permission from ref 36. Copyright 2010 American Chemical Society. Reprinted with permission from ref 37. Copyright 2008 American Institute of Physics.

isotropic; however, other properties, such as superconductivity,[32] ferromagnetism,[33] and quantum Hall effect[34] are closely related to their localized edge states and are edge-dependent. In this section, we will discuss the methods of Raman spectroscopy to identify the edge types of isotropic 2D materials using graphene as an example.

The intensity of the G mode of graphene has been proposed to identify the orientation of the edge.[36−38] The G band is the first-order Raman mode originating from the iTO and iLO phonons (with the E_{2g} symmetry) at the center of the first Brillouin zone. The Raman tensors of the G mode can be described as

$$\tilde{R}(E_{2g}(1)) = \begin{pmatrix} 0 & d & 0 \\ d & 0 & 0 \\ 0 & 0 & 0 \end{pmatrix} \text{ and } \tilde{R}(E_{2g}(2)) = \begin{pmatrix} d & 0 & 0 \\ 0 & -d & 0 \\ 0 & 0 & 0 \end{pmatrix}$$

$$(6)$$

According to the Raman selection rules, the Raman intensity of G mode in the center of the graphene sheet shows no polarization dependence. In contrast, opposite polar behaviors of the armchair edge and zigzag edge have been reported and proven to be an effective way to identify the type of graphene edges.[36−38]

Figure 2a−d shows different polarization dependence for armchair and zigzag edges of graphene. The Raman intensity of the G band becomes lower (higher) with the increase of the angle between incident polarization light and armchair (zigzag) edge, as shown in the Figure 2a,c. Further study showed that $\cos^2 \theta$ can be employed to fit the angle dependence of intensities of armchair edges (Figure 2b), and $\sin^2 \theta$ can be employed for zigzag edges (Figure 2d). The different polarization dependence comes from the degeneration of the iTO and iLO phonons for the armchair and zigzag edges. Specifically, only the iLO phonons are active in the armchair edges, whereas only the iTO phonons are active in the zigzag edges. Therefore, the different polarization dependence can be understood through different Raman tensors and different selection rules of iTO and iLO phonons in the armchair and zigzag edges.[36]

The D peak at near 1350 cm^{-1} originates from the double-resonance Raman process involving the scattering by defects. The intensity of the D peak disappears for high-quality graphene and is very high for amorphous carbon. The orientation of edges can also be characterized through the D band intensities. Theoretical studies show that the double-resonance process of D mode can be fulfilled only at armchair edges, while it is forbidden for zigzag edges.[33] In other words, the D band is strong for armchair edges while weaker or even absent for zigzag edges.[39] For example, Figure 2e shows the Raman images of D and G band of a graphene sheet, where the different D band contrast of the two edges can be clearly seen.[37] In summary, armchair and zigzag edges can also be distinguished from the different polarization-dependence of the D band.

The G band splits to G$^+$ sub-band and G$^-$ sub-band under strain, which can also be used to characterize the orientation of graphene. Experiments show that the G band red-shifts and the splitting increases as the strain increases. The two splitting G sub-bands correspond to two orthogonal modes: G$^+$ sub-band is assigned as E_{2g}^+ with carbon atom vibration perpendicular to the strain, while G$^-$ sub-band is E_{2g}^- with vibration parallel to the strain. For a graphene sheet under a uniaxial compressive strain, the C═C bonds parallel to the strain will be shortened and hardened, leading to significant red-shift of the G$^-$ sub-band, while the bonds perpendicular to the strain will be only slightly affected and the G$^+$ sub-band is slightly shifted.[40]

The intensities of G$^+$ and G$^-$ sub-bands under the uniaxial strain are dependent on the incident laser polarization. Figure 3a shows the Raman spectra of the two sub-bands under different incident laser polarization. The polar plots of G$^+$ and G$^-$ intensity are shown in Figure 3b, in which the data can be fitted by $I_{G^+} \propto \sin^2(\theta_{in} + 34°)$ and $I_{G^-} \propto \cos^2(\theta_{in} + 34°)$. Theoretical results[34] show that the relative intensity of the two sub-bands can be expressed as

$$\frac{I_{G^-}}{I_{G^+}} = \tan^2(\theta_{in} + \theta_{out} + 3\phi_s)$$
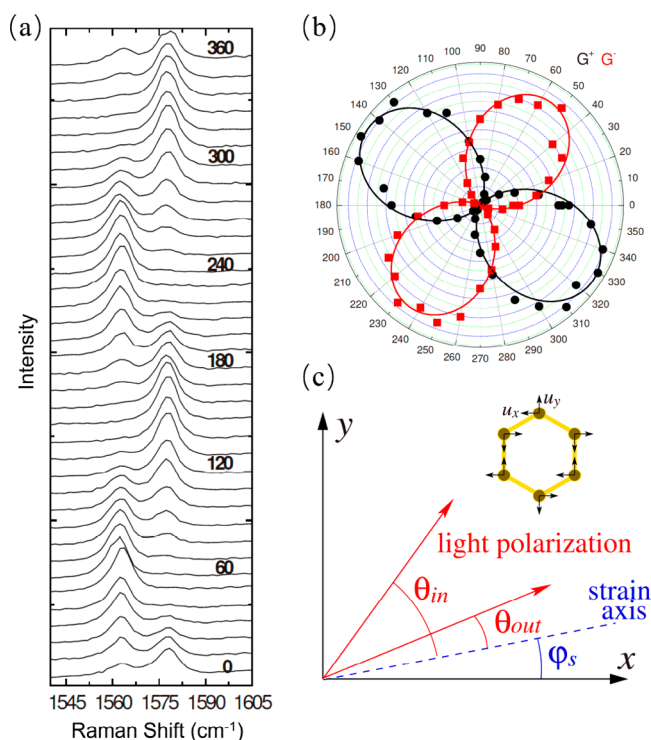
$$(7)$$

(a)

(b)

(c)

Figure 3. (a) Raman spectra of G^+ and G^- sub-band with different angles between incident light polarization and the applied strain. (b) Polar plot of the G^+ and G^- intensity as a function of the angle between incident light polarization and the applied strain. The analyzer is placed parallel to the strain axis. (c) Corresponding polarization geometry. The hexagon represents the lattice of graphene and the dark circles are the carbon atoms. The short black arrows represent phonon displacements in the x and y axis.[40] Reprinted with permission from ref 40. Copyright 2009 American Physical Society.

where θ_{in}, θ_{out}, and ϕ_s represent the angle between incident laser polarization and the strain axis, the angle between the analyzer and the strain axis, and the angle between the strain axis and the graphene crystal axis, as illustrated in Figure 3c. Therefore, the angle ϕ_s can be calculated through fitting the experimental data, and the crystallographic orientation of graphene can be easily obtained.[40]

Similarly, the 2D band red-shifts and splits to $2D^+$ and $2D^-$ sub-bands under strain too, which can be explained as a deformation of the Dirac cone and a displacement away from the K point of the graphene Brillouin zone. The intensities also depend on the direction of both incident laser and analyzer and graphene orientation as well, which can be used to detect the direction of graphene orientation.[41]

These methods can also be employed to characterize the crystallographic orientation of other two-dimensional materials with in-plane isotropy. For example, the E_{2g}^1 mode of MoS_2 shows obvious red-shifts and splits into E_{2g}^{1+} and E_{2g}^{1-} modes when increasing strain like the G mode of graphene. The intensities of the two modes orthogonally respond to the angle between the direction of the analyzer and the strain axis, which can be adopted to identify the crystallographic orientation of MoS_2.[35]

In-plane anisotropic 2D materials possess crystallographic orientation-dependent optical, electronic, thermal, and mechanical properties.[42,43] The rapid and efficient characterization of their crystallographic orientation is important for both fundamental studies and device applications. In-plane

anisotropic 2D materials usually have crystal structures belonging to orthorhombic (BP, SnS, SnSe, *etc*), monoclinic (T'-MoTe$_2$, ZrTe$_3$, *etc*) and triclinic crystal system (ReS$_2$, ReSe$_2$, *etc*).[3] In this section, we will discuss the methods of ARPRS to identify the crystallographic orientation of anisotropic 2D materials using BP as an example. It should be noted that there are more factors to be considered when reducing crystal symmetry in comparison with BP.

Bulk BP belongs to orthorhombic crystal system (D_{2h}) and the primitive unit cell of monolayer BP includes 4 atoms (Figure 4a). It follows that there are 12 normal vibration modes at the Γ point of its Brillouin zone. Among these modes, A$_g$, B$_{1g}$, B$_{2g}$, and B$_{3g}$ modes are Raman-active, and only A$_g$ and B$_{2g}$ modes could be observed under backscattering configuration. As we can see from Figure 4a, the representative Raman spectrum of a few-layer BP sample shows three Raman peaks, that is, A$_g^1$ (366.3 cm^{-1}), B$_{2g}$ (440.7 cm^{-1}), and A$_g^2$ (467 cm^{-1}) modes. They correspond to intralayer modes in BP, and their atomic displacements are illustrated in Figure 4b−d. P atoms for A$_g^1$ mode mainly vibrate in the out-of-plane direction, while the A$_g^2$ mode is dominated by atomic vibrations along the in-plane armchair direction. B$_{2g}$ is also in-plane vibration mode with atoms vibrating along the zigzag direction.

According to the Raman selection rule, polarized Raman spectroscopy can be used to identify the crystalline orientations of anisotropic crystal BP. Specifically, the Raman tensors for A$_g$ mode and B$_{2g}$ mode in BP have the general form of

$$\tilde{R}(A_g) = \begin{pmatrix} a & 0 & 0 \\ 0 & b & 0 \\ 0 & 0 & c \end{pmatrix} \tag{8}$$

$$\tilde{R}(B_{2g}) = \begin{pmatrix} 0 & 0 & e \\ 0 & 0 & 0 \\ e & 0 & 0 \end{pmatrix} \tag{9}$$

According to the Raman selection rules such as eq 1, angle-dependent polarized Raman intensities with rotating samples follow the relationship with θ as (the calculation details can be seen in ref 30)

$$I_{\|A_g} \propto (a\cos^2\theta + c\sin^2\theta)^2 \tag{10}$$

$$I_{\|B_{2g}} \propto e^2 \sin^2 2\theta \tag{11}$$

$$I_{\perp A_g} \propto (a-c)\sin^2\theta\cos^2\theta \tag{12}$$

$$I_{\perp B_{2g}} \propto e^2\cos^2 2\theta \tag{13}$$

where θ is the angle between the incident polarization and armchair direction of BP; $I_{\|}$ is the Raman intensity under parallel polarization (VV), and $I_{\perp}$ is the Raman intensity under perpendicular polarization (VH). Hence the intensities of both A$_g$ and B$_{2g}$ modes are closely related to the actual sample orientation. For example, when the incident polarization is along the zigzag direction where $\theta = 90°$ (or armchair direction where $\theta = 0°$), $I_{\|A_g}$ is proportional to c^2 (or a^2) and $I_{\perp A_g}$ is 0. For both configurations, $I_{\|B_{2g}}$ is 0 while $I_{\perp B_{2g}}$ is proportional to e^2. Consequently, the angle-dependent Raman intensities could be used to identify the crystalline orientation of BP. As shown
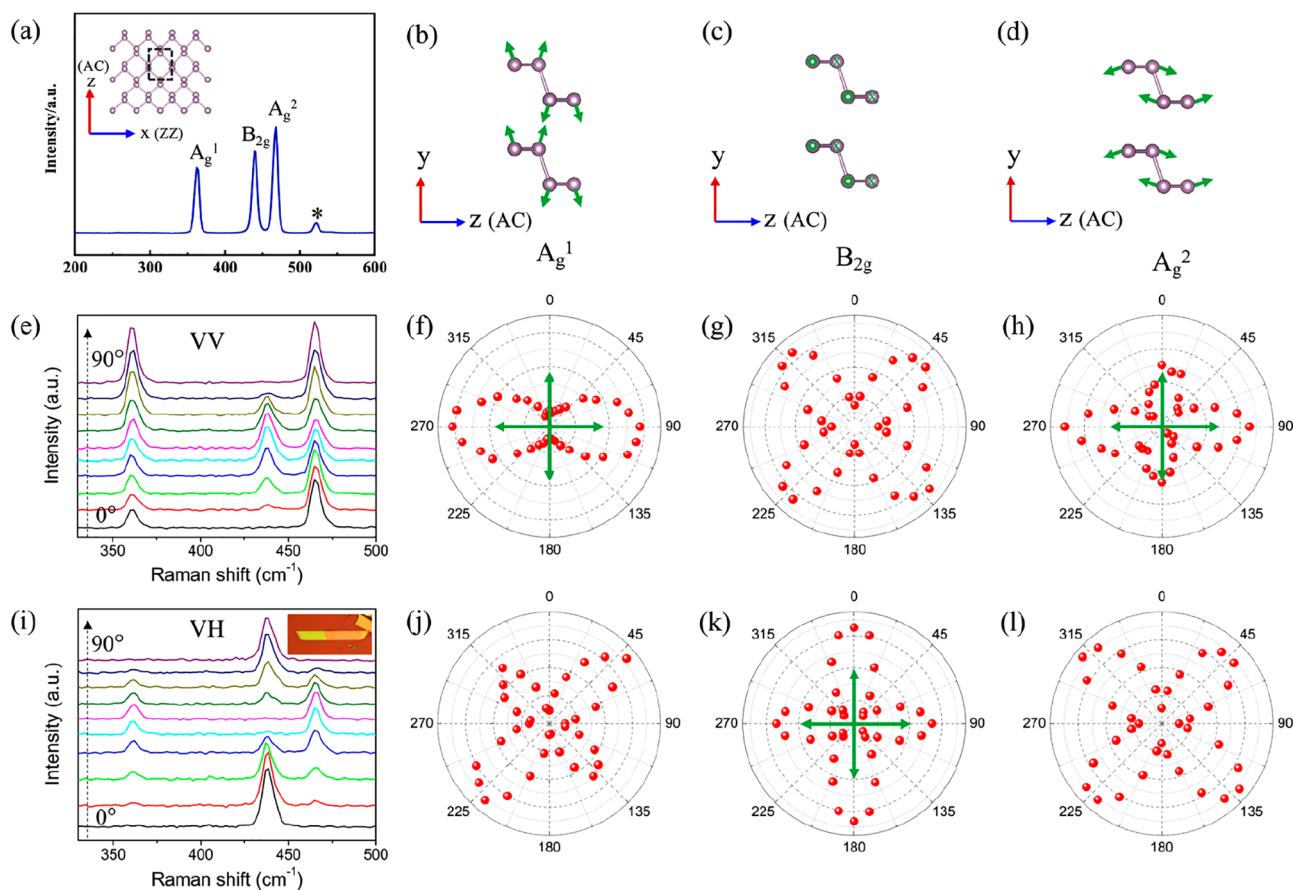
Figure 4. (a) Raman spectra of a few-layer BP sample. Si peak at 520.7 cm^{-1} is marked with asterisk. The inset is the atomic structure of monolayer BP. Its unit cell is represented by the rectangular region. (b−d) The atomic displacements of A_g^1, B_{2g}, and A_g^2 modes in BP. (e−h) Angle-dependent Raman spectra of bulk BP under parallel (e−h) and perpendicular polarization configurations (i−l). Green arrows indicate the crystalline orientations of BP.[30] Reprinted with permission from ref 30. Copyright 2015 Wiley.
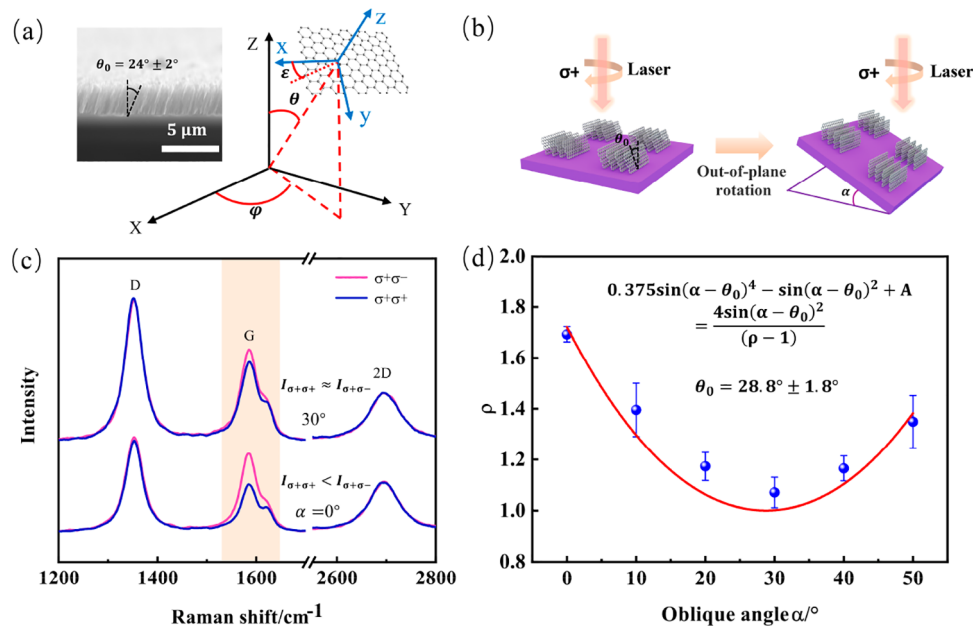

Figure 5. (a) Three-dimensional orientation of a graphene sheet can be expressed by the Euler angle (θ, φ, ε). The left part is the cross-sectional SEM of a vertical graphene (VG) array with an oblique angle θ_0. (b) Schematic of tilting the substrate with an angle α. The graphene sheets in the right are vertical to the horizontal plane. (c) Helicity-resolved Raman spectra of the sample with tilting angle 0° and 30°. (d) Correlation of circular polarization ratio ρ for G mode with the tilting angle α. The formula inside is used to fit the data.[25] Reprinted with permission from ref 25. Copyright 2021 American Chemical Society.

in Figure 4(e-l), the Raman spectra of bulk BP are indeed very sensitive to the sample rotation angle under both parallel and perpendicular polarization. Both A_g^1 and A_g^2 show local maximum intensities when the incident polarization is along the crystalline orientations of BP under parallel polarization, where either one could be the global maximum intensity, depending on a^2/c^2 (Figure 4f,h). The B_{2g} mode has its maximum intensity with the incident polarization along the crystalline orientations of BP under perpendicular polarization (Figure 4k).

It is worth noting that the a^2/c^2 ratio for the A_g mode is dependent on the thickness of the BP sample and excitation energy. The dependence of the a^2/c^2 ratio on the sample thickness and excitation energies is mainly attributed to the intrinsic anisotropic electron−photon and electron−phonon coupling in BP, thickness-dependent electronic band structure evolution, and interference effect.[44]

It should be noted that the Raman intensity polar plot of totally symmetric A_g mode actually cannot be fitted nicely with the formula deduced from the Raman selection rule quantitatively. Two models were propsed to explain the abnormal polarized Raman selection rule. One is the semiempirical model considering the complex Raman tensor,[44,45] and the other is based on the birefringence effect and linear dichroism of BP.[46,47]

BP is the simplest biaxial crystal, acting as a prototype of anisotropic 2D materials. The discussions in this section on identifying the crystalline orientations of BP using polarized Raman spectroscopy and models to explain the abnormal angle-dependent Raman intensities are generally applicable to other anisotropic 2D crystals.[8,48]

For macro materials assembled from units of nanomaterials, the performance is strongly dependent on the orientation of the unit nanomaterials. Hence, the fast and *in situ* characterization of the orientation distribution is of urgent need.

Vertical graphene (VG) arrays have been considered as a promising candidate of thermal interface materials because the in-plane thermal conductivity of graphene is extremely high.[49] The oblique angle (out-of-plane orientation) is an important factor for the thermal conductivity of VG arrays.[18,50] Recently, we developed a technique of helicity-resolved Raman spectroscopy (HRRS) to quantitatively characterize the oblique VG arrays, which proved to be simpler and more reliable than the conventional linearly polarized spectroscopy.[25]

The three-dimensional orientation of graphene sheet can be expressed by the Euler angle $(\theta, \varphi, \varepsilon)$, as shown in Figure 5a. According to the Raman selection rules, the Raman intensities of G mode for a graphene sheet can be written as

$$I_{\sigma^+\sigma^+} \propto (\cos\theta^2 - 1)^2 = \sin\theta^4 \qquad (14)$$

$$I_{\sigma^+\sigma^-} \propto (\cos\theta^2 + 1)^2 + 4\cos\theta^2 \qquad (15)$$

$I_{\sigma^+\sigma^+}$ represents the intensity of helicity-conserved Raman scattering, and $I_{\sigma^+\sigma^-}$ is the intensity of helicity-changed scattering. One thing to notice is that the intensities under $(\sigma^+\sigma^+)$ and $(\sigma^+\sigma^-)$ configurations depend on only out-of-plane angle θ (oblique angle). For VG arrays with an oblique angle θ_0, if assuming that the in-plane angle φ is arbitrary, the relationship between oblique angle θ_0, the tilting angle α (Figure 5b), and the circular polarization ratio $(\rho = \frac{I_{\sigma^+\sigma^-}}{I_{\sigma^+\sigma^+}})$ can be expressed as

$$0.375\sin(\alpha - \theta_0)^4 - \sin(\alpha - \theta_0)^2 + A = \frac{4\sin(\alpha - \theta_0)^2}{(\rho - 1)} \qquad (16)$$

where A is a constant representing equal intensities of $I_{\sigma^+\sigma^+}$ and $I_{\sigma^+\sigma^-}$, which may come from impurities like amorphous carbon.

The left part in Figure 5a is the cross-sectional scanning electron microscopy (SEM) image of a VG array with an oblique angle θ_0, which was measured by SEM to be $24° \pm 2°$. In order to measure the oblique angle θ_0 through HRRS, the VG array has been tilted by an angle α as shown in Figure 5b. The corresponding HRRS is shown in Figure 5c, which indicates that $I_{\sigma^+\sigma^+} < I_{\sigma^+\sigma^-}$ for tilting angle $0°$, while $I_{\sigma^+\sigma^+} \approx I_{\sigma^+\sigma^-}$ for tilting angle $30°$. The oblique angle can be characterized accurately by fitting α-dependent circular polarization ratio (Figure 5d) using eq 16. We can get $\theta_0 = 28.8° \pm 1.8°$ and $A = 1.49$ from curve fitting, which means the error is less than $5°$ compared with the value measured by SEM. The result implies that the HRRS technique is highly reliable and accurate for the determination of out-of-plane orientation. The HRRS can be extended to various nanomaterials assemblies, and if combined with ARPRS, the characterization of three-dimensional orientation for more complex system can be implemented.

For nanomaterial assemblies like fibers of single-walled carbon nanotubes (SWNTs), polymers, or polymer nano-composites reinforced by graphene/SWNTs, it is necessary to introduce the orientation distribution function (ODF) to describe the orientation distribution of nanomaterials assemblies. In this section, we will introduce the basic theory of ODF as well as the orientation distribution coefficients P_{lmn} for the specimen with uniaxial symmetry; we then will give practical applications of ODF for the Raman spectroscopic study of typical sample with uniaxial orientation.

According to the study of Bower,[22] the orientation distribution function $N(\theta, \varphi, \varepsilon)$ is introduced to describe molecular orientation distribution, in which $N(\theta, \varphi, \varepsilon)\sin\theta \, d\theta \, d\varphi \, d\varepsilon$ denotes the fraction of scattering units having orientation within a solid angle $\sin\theta \, d\theta \, d\varphi \, d\varepsilon$. The function $N(\theta, \varphi, \varepsilon)$ can be written by the following equation as a function of $\cos\theta$:

$$N(\theta, \varphi, \varepsilon) = \sum_{l=0}^{\infty} \sum_{m=-l}^{l} \sum_{n=-l}^{l} v_{lmn} Z_{lmn}(\cos\theta) e^{-im\varepsilon} e^{-in\varphi}$$
$$= \sum_{lmn} v_{lmn} Z_{lmn}(\cos\theta) e^{-im\varepsilon} e^{-in\varphi} \qquad (17)$$

where the term v_{lmn} and Z_{lmn} are the expansion coefficients and the lmn orders generalized Legendre polynomials, respectively (more details about ODF can also be found in ref 6).

> Raman spectroscopy can be compared with other techniques such as X-ray diffraction and birefringence measurements for determining molecular orientation distributions.

It is important that polarized Raman spectroscopy can be compared with other techniques such as X-ray diffraction and birefringence measurements for determining molecular orientation distributions. In these techniques, the molecular
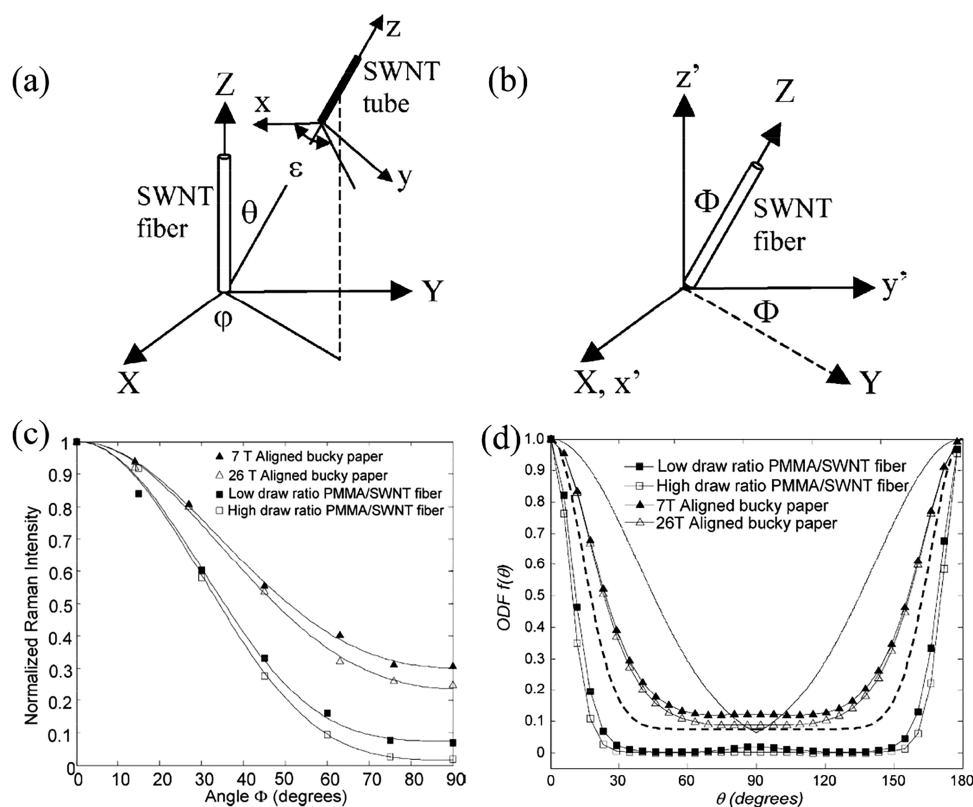
Figure 6. Schematic orientation representation of SWNTs in a SWNT fiber (a) and the fiber arrangement in the lab coordinate system O-$x'y'z'$(b). Z is the SWNT fiber axis, and z is the SWNT tube axis. (c) Normalized Raman scattering intensity of magnetic field aligned bucky paper and PMMA/SWNT composite fiber. (d) Orientation distribution functions (ODF) of SWNTs in various SWNT bulk samples constructed with the orientation parameters $\langle P_{200}(\cos\theta)\rangle$ and $\langle P_{200}(\cos\theta)\rangle$.[7] Reprinted with permission from ref 7. Copyright 2003 Elsevier.

orientation distributions are usually described by molecular orientation distribution coefficients P_{lmn}, where l, m, and n are integers. The details discussed in this section will be mainly for a specimen with uniaxial symmetry for which the calculation can be much simplified.

For a sample with uniaxial symmetry, the P_{lmn} values are nonzero only when $m = n = 0$ and l is even, and they are related with the ODF $f(\theta)$ as[6]

$$\langle P_{l00}\rangle = \frac{\int_0^\pi f(\theta)P_{l00}(\cos\theta)\sin\theta\,d\theta}{\int_0^\pi f(\theta)\sin\theta\,d\theta} \tag{18}$$

The θ here represents the angle between the z-axis of the specimen coordinates and Z-axis of the laboratory coordinates, as shown in the right of Figure 6. $\langle P_{l00}\rangle$ here means the average values of $P_{l00}(\cos\theta)$. The $P_{l00}(\cos\theta)$ are Legendre polynomial functions of $\cos\theta$.

Therefore, for a uniaxial-oriented specimen, the ODF $f(\theta)$ can be expressed by the orientation distribution coefficients $P_{l00}(\cos\theta)$:[51]

$$f(\theta) = \sum_{l=0}^{\infty}\left(\frac{2l+1}{2}\right)\langle P_{l00}\rangle P_{l00}(\cos\theta) \tag{19}$$

In practice, a diversity of materials has been examined using the orientation distribution function for the evaluation of molecular orientation distribution, as well as for the conformational and microstructure study.[6] In recent years, the technique is still quite open for more materials, such as D-FF molecule within a nanotube and various nano-carbon materials.[7,52−54] In

this section, we will discuss the practical applications of ODF for the study of orientations of carbon nanomaterials, taking SWNT fiber as an example.

A generalized spherical harmonics expanded ODF has been used to study the orientation of SWNTs by Liu and Kumar in 2003.[7] For an individual SWNT, its orientation related to the XYZ coordinate fixed onto bulk sample can be described by three Euler's angles $(\theta, \varphi, \varepsilon)$, as shown in Figure 6a. Moreover, the $f(\theta,\ \varphi,\ \varepsilon)\sin\theta\,d\theta\,d\varphi\,d\varepsilon$ represents the probability of locating an individual nanotube with the orientation between $(\theta, \varphi, \varepsilon)$ and $(\theta + d\theta,\varphi + d\varphi, \varepsilon + d\varepsilon)$. An arbitrary ODF $f(\theta, \varphi, \varepsilon)$ can be expressed by a series of generalized spherical functions according to a previous section. However, the expression of ODF can be simplified greatly because SWNTs possess cylindrical symmetry and only uniaxial orientation has been considered here. For such cases, the ODF can be given by eq 19.

Because of the resonance enhancement of Raman scattering, the Raman intensity of SWNT is determined by its polarizability tensor rather than the Raman tensor (the derivation of the polarization tensor).[7]

$$I \propto |\vec{e}_s(\Phi)\cdot\tilde{\alpha}(\theta,\ \varphi,\ \varepsilon)\cdot\vec{e}_i(\Phi)|^2 \tag{20}$$

Because of the angle-dependent resonance enhancement, the polarizability tensor α of the SWNT in its principal coordinate is dominated by the component parallel to the tube axis (α_{zz}). The polarization tensor $\tilde{\alpha}$ is approximated by
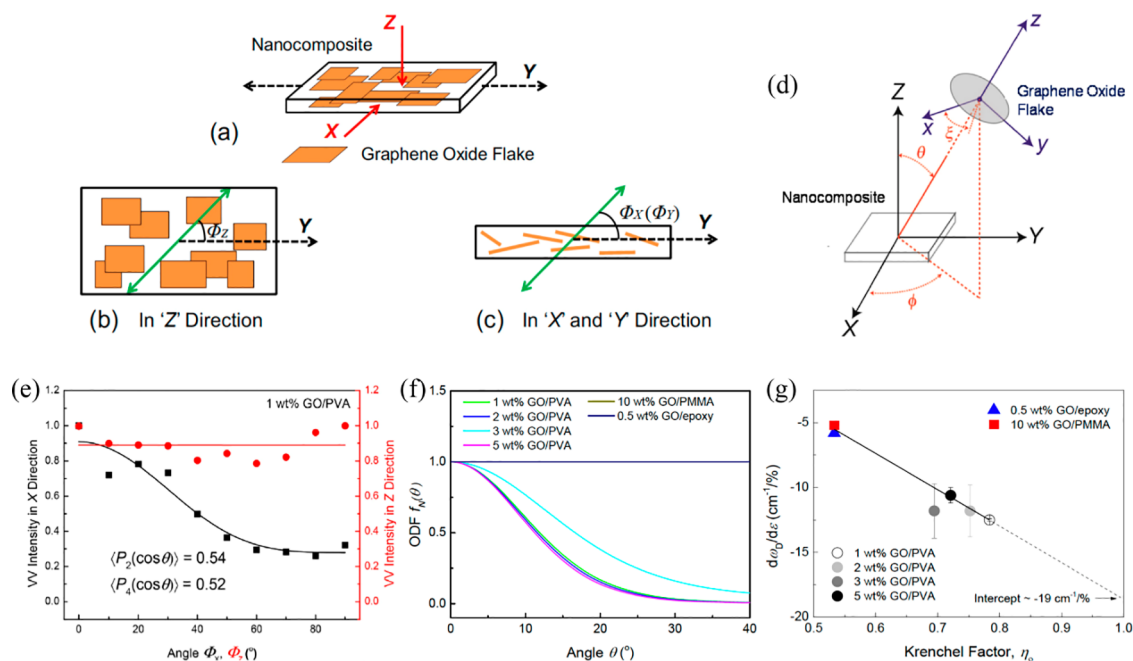
Figure 7. (a) Schematic illustration of the Cartesian coordinate system with the sample geometries used in the Raman spectroscopic analysis in the three directions. (b) View with the laser beam along the Z axis. (c) View with the laser beam along the X and Y axes. The red arrows represent the laser propagation directions, and the green arrows represent the directions of polarization of the incident and scattered light. (d) Relationship between the coordinate systems of the GO flake (x, y, z) and the nanocomposite sample (X, Y, Z), which is defined by Euler angles $(\theta, \varphi, \varepsilon)$. (e) I_G variation with angle Φ for GO/PVA nanocomposites with the laser beam in X (black) and Z (red) directions. (f) Orientation distribution functions (ODFs) for the studied materials. (g) Correlation of the Krenchel factor η_0 with the reported $d\omega_D/d\varepsilon$ of GO/PVA (black circle), GO/epoxy (blue triangle), and GO/PMMA (red square).[54] Reprinted with permission from ref 54. Copyright 2016 Elsevier.

$$\tilde{\alpha} = \begin{pmatrix} \alpha_{xx} & 0 & 0 \\ 0 & \alpha_{yy} & 0 \\ 0 & 0 & \alpha_{zz} \end{pmatrix} = \begin{pmatrix} 0 & 0 & 0 \\ 0 & 0 & 0 \\ 0 & 0 & 1 \end{pmatrix} \quad (21)$$

Therefore, the Raman intensity for an individual SWNT can be expressed as

$$I_{SWNT}^{VV} \propto [\cos\theta\cos\phi - \sin\theta\sin\phi\sin\varphi]^4 \quad (22)$$

$$I_{SWNT}^{VH} \propto [\cos\theta\cos\phi - \sin\theta\sin\phi\sin\varphi]^2 \\ \times [\cos\theta\sin\phi + \sin\theta\cos\phi\sin\varphi]^2 \quad (23)$$

where ϕ represents the angle between the polarization of incident light and the tube axis.

Taking the sum of the intensity of all SWNTs with different orientations, the Raman intensity of the SWNT fiber can be calculated by integration:

$$I_{SWNT}^{VV} \propto \left(\cos^4\Phi - \frac{6}{7}\cos^2\Phi + \frac{3}{35} \right)\langle P_4(\cos\theta)\rangle \\ + \left(\frac{6}{7}\cos^2\Phi - \frac{2}{7} \right)\langle P_2(\cos\theta)\rangle + \frac{1}{5} \quad (24)$$

$$I_{SWNT}^{VH} \propto \left(-\cos^4\Phi + \cos^2\Phi - \frac{4}{35} \right)\langle P_4(\cos\theta)\rangle \\ + \frac{1}{21}\langle P_2(\cos\theta)\rangle + \frac{1}{15} \quad (25)$$

It should be noted that only the second- and fourth-order orientation parameters appear in eqs 24 and 25, specifically, $\langle P_2(\cos\theta)\rangle = \langle P_4(\cos\theta)\rangle = 1$ for a specimen with SWNTs

perfectly aligned, while $\langle P_2(\cos\theta)\rangle = \langle P_4(\cos\theta)\rangle = 0$ for randomly aligned SWNTs. Figure 6c is the normalized Raman intensities of aligned bucky paper and a PMMA/SWNT composite fiber. The orientation parameters up to fourth order through ARPRS are shown in Figure 6c. Moreover, a complete orientation distribution function can be derived through $\langle P_2(\cos\theta)\rangle$ and $\langle P_4(\cos\theta)\rangle$, by following the maximum entropy formalism:

$$f(\theta) = A\exp[-(\lambda_2 P_2(\cos\theta) + \lambda_4 P_4(\cos\theta))] \quad (26)$$

Figure 6d shows the ODF coefficients of PMMA/SWNT fiber and bucky paper, which indicates that most SWNTs' orientations are below 30° for PMMA/SWNT fiber while a lower orientation of SWNTs in a magnetic field aligned bucky paper can be seen.

In addition to one-dimensional carbon nanotubes, the ODF of two-dimensional graphene has been studied widely.[53,54] Young[53,54] has quantified the three-dimensional spatial orientation of high-ordered pyrolytic graphite and graphene paper as well as the GO flakes in different nanocomposites, in terms of a generalized spherical expanded harmonics ODF based on the model Liu and Kumar developed. The spectra were obtained from both the transverse sections and the top surfaces of the graphene using the VV polarization, as shown in Figure 7a−c. Similarly, the three-dimensional orientation of graphene can be expressed by Euler's angle $(\theta, \varphi, \varepsilon)$, as shown in Figure 7d. Figure 7e presents I_G variation with angle Φ for GO/PVA nanocomposites with the laser beam in X (black) and Z (red) directions, from which we can see that I_G is independent of ϕ_Z in the case of the direction of laser parallel to the Z axis, while there is a strong dependence of I_G on the angle ϕ_X in the transverse section. Similar to the model of

carbon nanotubes above, the Raman scattered intensity of a specimen like GO/PMMA for the polarization angle Φ relative to the sample can be expressed as

$$I_G^{VV} \propto \left(\cos^4\Phi - \frac{8}{7}\cos^2\Phi + \frac{8}{35}\right)\langle P_4(\cos\theta)\rangle$$
$$+ \left(\frac{8}{7}\cos^2\Phi - \frac{16}{21}\right)\langle P_2(\cos\theta)\rangle + \frac{8}{15} \quad (27)$$

The $\langle P_2(\cos\theta)\rangle$ and $\langle P_4(\cos\theta)\rangle$ can be derived from the Raman intensity as shown in Figure 7e, and the ODF as indicated previously in eq 19 can be obtained as shown in Figure 7f.

One of the most important applications of the order parameters $\langle P_2(\cos\theta)\rangle$ and $\langle P_4(\cos\theta)\rangle$ is to determine the Krenchel orientation factor η_0 which defines the effect of the orientation of materials like graphene upon the mechanical properties of reinforced composites. For example, $\eta_0 = 1$ for perfectly aligned nanotubes, but $\eta_0 = 3/8$ for nanotubes oriented randomly in 2D plane and $\eta_0 = 1/5$ for 3D composites.[13] For a single reinforcement element

$$\eta_0 = \cos^4\zeta \quad (28)$$

where ζ is the angle between the element orientation and the axis the stress applied. Through the integration over the ODF, the Krenchel factor η_0 can be written as

$$\eta_0 = \frac{3}{35}\langle P_4(\cos\theta)\rangle + \frac{8}{21}\langle P_2(\cos\theta)\rangle + \frac{8}{15} \quad (29)$$

It is significant that η_0 depends only on $\langle P_2(\cos\theta)\rangle$ and $\langle P_4(\cos\theta)\rangle$ and hence can be directly determined by ARPRS. The effective Young's modulus of the GO in nanocomposites can be derived from the D band shift rate with strain ($d\omega_D/d\varepsilon$). The linear relationship between the converted $d\omega_D/d\varepsilon$ and η_0 can be seen from the Figure 7g, which links the degree of spatial orientation of reinforcement with the mechanical properties of nanocomposites.

Polarized Raman spectroscopy has been widely used to determine the crystallographic orientation of various low-dimensional nanomaterials. In this Perspective, we introduce the basic principles as well as the experimental setups, then the specific methods to characterize crystallographic orientation of a series of 2D materials are discussed in detail. Furthermore, the orientation distribution function is introduced to describe the orientation of nanomaterial assemblies like CNT fibers in the last section.

First, abnormal polarized Raman selection rules by considering complex Raman tensor or optical birefringent

> Polarized Raman spectroscopy has made tremendous progress in recent years and has become a mature tool to characterize crystallographic orientation of various low-dimensional nanomaterials. However, there still exist several challenges in both the theoretical model and practical characterization.

effect have been reported for some in-plane anisotropic 2D materials like BP or ReS_2. This makes the determination of crystallographic orientation more complicated because the selection rules after correction are related to the excitation wavelength and the layer numbers of 2D materials. Second, most of the orientation characterization methods apply only to in-plane orientation. However, the spatial orientation in three-dimensions is also of great significance for nanomaterials such as molecular films or nanomaterial arrays, and the characterization of spatial orientation retains great challenges to date. Third, the orientation distribution function is a useful model to describe the orientation of nanomaterial assemblies, which can then be linked to the orientation with their device performance. However, the calculation is still too complicated, especially for specimens without uniaxial symmetry, and needs simplification. On the other hand, an oversimplified ODF will lose some orientation information. The ODF model requires further optimization for more orientation characterization of materials without uniaxial symmetry. Last but not least, circularly polarized Raman spectroscopy provides an opportunity to study the out-of-plane orientation of nanomaterials, and theoretical models that combine circular and linear polarization in Raman scattering should be developed and may have high impact for the study of spatial orientation in three dimensions.

■ AUTHOR INFORMATION

Corresponding Authors

Lianming Tong − *Center for Nanochemistry, Beijing Science and Engineering Center for Nanocarbons, Beijing National Laboratory for Molecular Sciences, College of Chemistry and Molecular Engineering, Peking University, Beijing 100871, P.R. China;* ⊙ orcid.org/0000-0001-7771-4077; Email: tonglm@pku.edu.cn

Jin Zhang − *Center for Nanochemistry, Beijing Science and Engineering Center for Nanocarbons, Beijing National Laboratory for Molecular Sciences, College of Chemistry and Molecular Engineering, Peking University, Beijing 100871, P.R. China;* ⊙ orcid.org/0000-0003-3731-8859; Email: jinzhang@pku.edu.cn

Authors

Bo Xu − *Academy for Advanced Interdisciplinary Studies, Peking University, Beijing 100871, P.R. China; Center for Nanochemistry, Beijing Science and Engineering Center for Nanocarbons, Beijing National Laboratory for Molecular Sciences, College of Chemistry and Molecular Engineering, Peking University, Beijing 100871, P.R. China*

Nannan Mao − *Department of Electrical Engineering and Computer Science, Massachusetts Institute of Technology, Cambridge, Massachusetts 02139, United States;* ⊙ orcid.org/0000-0003-3522-5341

Yan Zhao − *Academy for Advanced Interdisciplinary Studies, Peking University, Beijing 100871, P.R. China; Center for Nanochemistry, Beijing Science and Engineering Center for Nanocarbons, Beijing National Laboratory for Molecular Sciences, College of Chemistry and Molecular Engineering, Peking University, Beijing 100871, P.R. China*

Complete contact information is available at:
https://pubs.acs.org/10.1021/acs.jpclett.1c01889

Notes

The authors declare no competing financial interest.

■ ACKNOWLEDGMENTS

■ REFERENCES

(1) Ferrari, A. C.; Basko, D. M. Raman Spectroscopy as a Versatile Tool for Studying the Properties of Graphene. *Nat. Nanotechnol.* **2013**, *8*, 235−246.

(2) Dresselhaus, M. S.; Dresselhaus, G.; Saito, R.; Jorio, A. Raman Spectroscopy of Carbon Nanotubes. *Phys. Rep.* **2005**, *409*, 47−99.

(3) Zhang, S. S.; Zhang, N.; Zhao, Y.; Cheng, T.; Li, X. B.; Feng, R.; Xu, H.; Liu, Z. R.; Zhang, J.; Tong, L. M. Spotting the Differences in Two-Dimensional Materials - the Raman Scattering Perspective. *Chem. Soc. Rev.* **2018**, *47*, 3217−3240.

(4) Godinho, R. B.; Santos, M. C.; Poppi, R. J. Quality Control of Fragrances Using Raman Spectroscopy and Multivariate Analysis. *J. Raman Spectrosc.* **2016**, *47*, 579−584.

(5) Nie, S. M.; Emery, S. R. Probing Single Molecules and Single Nanoparticles by Surface-Enhanced Raman Scattering. *Science* **1997**, *275*, 1102−1106.

(6) Tanaka, M.; Young, R. J. Polarised Raman Spectroscopy for the Study of Molecular Orientation Distributions in Polymers. *J. Mater. Sci.* **2006**, *41*, 963−991.

(7) Liu, T.; Kumar, S. Quantitative Characterization of SWNT Orientation by Polarized Raman Spectroscopy. *Chem. Phys. Lett.* **2003**, *378*, 257−262.

(8) Zhang, S. S.; Mao, N. N.; Zhang, N.; Wu, J. X.; Tong, L. M.; Zhang, J. Anomalous Polarized Raman Scattering and Large Circular Intensity Differential in Layered Triclinic ReS$_2$. *ACS Nano* **2017**, *11*, 10366−10372.

(9) Loudon, R. The Raman Effect in Crystals. *Adv. Phys.* **2001**, *50*, 813−864.

(10) Xu, S.; Zhang, J. Vertically Aligned Graphene for Thermal Interface Materials. *Small Structures* **2020**, *1*, 2000034.

(11) Liu, C.; Kong, D. S.; Hsu, P. C.; Yuan, H. T.; Lee, H. W.; Liu, Y. Y.; Wang, H. T.; Wang, S.; Yan, K.; Lin, D. C.; et al. Rapid Water Disinfection Using Vertically Aligned MoS$_2$ Nanofilms and Visible Light. *Nat. Nanotechnol.* **2016**, *11*, 1098−1104.

(12) Barth, J. V.; Costantini, G.; Kern, K. Engineering Atomic and Molecular Nanostructures at Surfaces. *Nature* **2005**, *437*, 671−679.

(13) Papageorgiou, D. G.; Li, Z. L.; Liu, M. F.; Kinloch, I. A.; Young, R. J. Mechanisms of Mechanical Reinforcement by Graphene and Carbon Nanotubes in Polymer Nanocomposites. *Nanoscale* **2020**, *12*, 2228−2267.

(14) Vigolo, B.; Penicaud, A.; Coulon, C.; Sauder, C.; Pailler, R.; Journet, C.; Bernier, P.; Poulin, P. Macroscopic Fibers and Ribbons of Oriented Carbon Nanotubes. *Science* **2000**, *290*, 1331−1334.

(15) Xin, G. Q.; Zhu, W. G.; Deng, Y. X.; Cheng, J.; Zhang, L. T.; Chung, A. J.; De, S.; Lian, J. Microfluidics-Enabled Orientation and Microstructure Control of Macroscopic Graphene Fibres. *Nat. Nanotechnol.* **2019**, *14*, 168−175.

(16) Coleman, J. N.; Khan, U.; Gun'ko, Y. K. Mechanical Reinforcement of Polymers Using Carbon Nanotubes. *Adv. Mater.* **2006**, *18*, 689−706.

(17) Gevorgyan, A. H.; Harutyunyan, M. Z. Chiral Photonic Crystals with an Anisotropic Defect Layer. *Phys. Rev. E* **2007**, *76*, 031701.

(18) Xu, S. C.; Wang, S. S.; Chen, Z.; Sun, Y. Y.; Gao, Z. F.; Zhang, H.; Zhang, J. Electric-Field-Assisted Growth of Vertical Graphene Arrays and the Application in Thermal Interface Materials. *Adv. Funct. Mater.* **2020**, *30*, 2003302.

(19) Xin, G. Q.; Yao, T. K.; Sun, H. T.; Scott, S. M.; Shao, D. L.; Wang, G. K.; Lian, J. Highly Thermally Conductive and Mechanically Strong Graphene Fibers. *Science* **2015**, *349*, 1083−1087.

(20) Chae, H. G.; Sreekumar, T. V.; Uchida, T.; Kumar, S. A Comparison of Reinforcement Efficiency of Various Types of Carbon Nanotubes in Poly Acrylonitrile Fiber. *Polymer* **2005**, *46*, 10925−10935.

(21) Wang, D. M.; Chen, G. R.; Li, C. K.; Cheng, M.; Yang, W.; Wu, S.; Xie, G. B.; Zhang, J.; Zhao, J.; Lu, X. B.; et al. Thermally Induced Graphene Rotation on Hexagonal Boron Nitride. *Phys. Rev. Lett.* **2016**, *116*, 126101.

(22) Bower, D. I. Investigation of Molecular Orientation Distributions by Polarized Raman-Scattering and Polarized Fluorescence. *J. Polym. Sci. Pt. B-Polym. Phys.* **1972**, *10*, 2135−2153.

(23) Liu, X.-L.; Zhang, X.; Lin, M.-L.; Tan, P.-H. Different Angle-Resolved Polarization Configurations of Raman Spectroscopy: A Case on the Basal and Edge Plane of Two-Dimensional Materials. *Chin. Phys. B* **2017**, *26*, 067802.

(24) Zhao, Y.; Zhang, S. S.; Shi, Y. P.; Zhang, Y. F.; Saito, R.; Zhang, J.; Tong, L. M. Characterization of Excitonic Nature in Raman Spectra Using Circularly Polarized Light. *ACS Nano* **2020**, *14*, 10527−10535.

(25) Xu, B.; Xu, S. C.; Zhao, Y.; Zhang, S. S.; Feng, R.; Zhang, J.; Tong, L. M. Determining the Oblique Angle of Vertical Graphene Arrays Using Helicity-Resolved Raman Spectroscopy. *J. Phys. Chem. C* **2021**, *125*, 8353−8359.

(26) Zheng, W.; Zheng, R. S.; Huang, F.; Wu, H. L.; Li, F. D. Raman Tensor of Aln Bulk Single Crystal. *Photonics Res.* **2015**, *3*, 38−43.

(27) Ding, Y.; Zheng, W.; Lu, X. F.; Liang, Y. L.; Zhu, Y. M.; Jin, M. G.; Huang, F. Raman Tensor of Layered SnS$_2$. *J. Phys. Chem. Lett.* **2020**, *11*, 10094−10099.

(28) Ding, Y.; Zheng, W.; Jin, M. G.; Zhu, Y. M.; Zhu, R. N.; Lin, Z. G.; Huang, F. Raman Tensor of Layered MoS$_2$. *Opt. Lett.* **2020**, *45*, 1313−1316.

(29) Zhu, Y. M.; Zheng, W.; Wang, W. L.; Zhu, S. Q.; Cheng, L.; Li, L. X.; Lin, Z. G.; Ding, Y.; Jin, M. G.; Huang, F. Raman Tensor of Layered Black Arsenic. *J. Raman Spectrosc.* **2020**, *51*, 1324−1330.

(30) Wu, J. X.; Mao, N. N.; Xie, L. M.; Xu, H.; Zhang, J. Identifying the Crystalline Orientation of Black Phosphorus Using Angle-Resolved Polarized Raman Spectroscopy. *Angew. Chem., Int. Ed.* **2015**, *54*, 2366−2369.

(31) Tatsumi, Y.; Saito, R. Interplay of Valley Selection and Helicity Exchange of Light in Raman Scattering for Graphene and MoS$_2$. *Phys. Rev. B: Condens. Matter Mater. Phys.* **2018**, *97*, 115407.

(32) Sasaki, K.; Jiang, J.; Saito, R.; Onari, S.; Tanaka, Y. Theory of Superconductivity of Carbon Nanotubes and Graphene. *J. Phys. Soc. Jpn.* **2007**, *76*, 033702.

(33) Nakada, K.; Fujita, M.; Dresselhaus, G.; Dresselhaus, M. S. Edge State in Graphene Ribbons: Nanometer Size Effect and Edge Shape Dependence. *Phys. Rev. B: Condens. Matter Mater. Phys.* **1996**, *54*, 17954−17961.

(34) Abanin, D. A.; Lee, P. A.; Levitov, L. S. Charge and Spin Transport at the Quantum Hall Edge of Graphene. *Solid State Commun.* **2007**, *143*, 77−85.

(35) Wang, Y. L.; Cong, C. X.; Qiu, C. Y.; Yu, T. Raman Spectroscopy Study of Lattice Vibration and Crystallographic Orientation of Monolayer MoS$_2$ under Uniaxial Strain. *Small* **2013**, *9*, 2857−2861.

(36) Cong, C. X.; Yu, T.; Wang, H. M. Raman Study on the G Mode of Graphene for Determination of Edge Orientation. *ACS Nano* **2010**, *4*, 3175−3180.

(37) You, Y. M.; Ni, Z. H.; Yu, T.; Shen, Z. X. Edge Chirality Determination of Graphene by Raman Spectroscopy. *Appl. Phys. Lett.* **2008**, *93*, 163112.

(38) Sasaki, K.; Saito, R.; Wakabayashi, K.; Enoki, T. Identifying the Orientation of Edge of Graphene Using G Band Raman Spectra. *J. Phys. Soc. Jpn.* **2010**, *79*, 044603.

(39) Casiraghi, C.; Hartschuh, A.; Qian, H.; Piscanec, S.; Georgi, C.; Fasoli, A.; Novoselov, K. S.; Basko, D. M.; Ferrari, A. C. Raman Spectroscopy of Graphene Edges. *Nano Lett.* **2009**, *9*, 1433−1441.

(40) Mohiuddin, T. M. G.; Lombardo, A.; Nair, R. R.; Bonetti, A.; Savini, G.; Jalil, R.; Bonini, N.; Basko, D. M.; Galiotis, C.; Marzari, N.;

et al. Uniaxial Strain in Graphene by Raman Spectroscopy: G Peak Splitting, Gruneisen Parameters, and Sample Orientation. *Phys. Rev. B: Condens. Matter Mater. Phys.* **2009**, *79*, 205433.

(41) Yoon, D.; Son, Y. W.; Cheong, H. Strain-Dependent Splitting of the Double-Resonance Raman Scattering Band in Graphene. *Phys. Rev. Lett.* **2011**, *106*, 155502.

(42) Qiao, J. S.; Kong, X. H.; Hu, Z. X.; Yang, F.; Ji, W. High-Mobility Transport Anisotropy and Linear Dichroism in Few-Layer Black Phosphorus. *Nat. Commun.* **2014**, *5*, 4475.

(43) Tran, V.; Soklaski, R.; Liang, Y. F.; Yang, L. Layer-Controlled Band Gap and Anisotropic Excitons in Few-Layer Black Phosphorus. *Phys. Rev. B: Condens. Matter Mater. Phys.* **2014**, *89*, 235319.

(44) Mao, N. N.; Wang, X. Z.; Lin, Y. X.; Sumpter, B. G.; Ji, Q. Q.; Palacios, T.; Huang, S. X.; Meunier, V.; Dresselhaus, M. S.; Tisdale, W. A.; et al. Direct Observation of Symmetry-Dependent Electron-Phonon Coupling in Black Phosphorus. *J. Am. Chem. Soc.* **2019**, *141*, 18994−19001.

(45) Ribeiro, H. B.; Pimenta, M. A.; de Matos, C. J. S.; Moreira, R. L.; Rodin, A. S.; Zapata, J. D.; de Souza, E. A. T.; Castro Neto, A. H. Unusual Angular Dependence of the Raman Response in Black Phosphorus. *ACS Nano* **2015**, *9*, 4270−4276.

(46) Mao, N. N.; Wu, J. X.; Han, B. W.; Lin, J. J.; Tong, L. M.; Zhang, J. Birefringence-Directed Raman Selection Rules in 2D Black Phosphorus Crystals. *Small* **2016**, *12*, 2627−2633.

(47) Lin, M. L.; Leng, Y. C.; Cong, X.; Meng, D.; Wang, J. H.; Li, X. L.; Yu, B. L.; Liu, X. L.; Yu, X. F.; Tan, P. H. Understanding Angle-Resolved Polarized Raman Scattering from Black Phosphorus at Normal and Oblique Laser Incidences. *Sci. Bull.* **2020**, *65*, 1894−1900.

(48) Wang, J. Y.; Luo, X.; Li, S. S.; Verzhbitskiy, I.; Zhao, W. J.; Wang, S. F.; Quek, S. Y.; Eda, G. Determination of Crystal Axes in Semimetallic T'-MoTe$_2$ by Polarized Raman Spectroscopy. *Adv. Funct. Mater.* **2017**, *27*, 1604799.

(49) Balandin, A. A. Thermal Properties of Graphene and Nanostructured Carbon Materials. *Nat. Mater.* **2011**, *10*, 569−581.

(50) Dai, W.; Ma, T. F.; Yan, Q. W.; Gao, J. Y.; Tan, X.; Lv, L.; Hou, H.; Wei, Q. P.; Yu, J. H.; Wu, J. B.; et al. Metal-Level Thermally Conductive yet Soft Graphene Thermal Interface Materials. *ACS Nano* **2019**, *13*, 11561−11571.

(51) Vangurp, M. The Use of Rotation Matrices in the Mathematical-Description of Molecular Orientations in Polymers. *Colloid Polym. Sci.* **1995**, *273*, 607−625.

(52) Sereda, V.; Ralbovsky, N. M.; Vasudev, M. C.; Naik, R. R.; Lednev, I. K. Polarized Raman Spectroscopy for Determining the Orientation of di-D-Phenylalanine Molecules in a Nanotube. *J. Raman Spectrosc.* **2016**, *47*, 1056−1062.

(53) Li, Z. L.; Young, R. J.; Kinloch, I. A.; Wilson, N. R.; Marsden, A. J.; Raju, A. P. A. Quantitative Determination of the Spatial Orientation of Graphene by Polarized Raman Spectroscopy. *Carbon* **2015**, *88*, 215−224.

(54) Li, Z. L.; Young, R. J.; Wilson, N. R.; Kinloch, I. A.; Valles, C.; Li, Z. Effect of the Orientation of Graphene-Based Nanoplatelets Upon the Young's Modulus of Nanocomposites. *Compos. Sci. Technol.* **2016**, *123*, 125−133.